

AD-A090 371

ARMY ARMAMENT RESEARCH AND DEVELOPMENT COMMAND DOVER--ETC F/6 19/1  
FULL FIELD INTERFEROMETRY APPLICATIONS TO ARMY PROBLEMS. (U)  
JUN 80 W K CADWALLENDER, K KRAMER

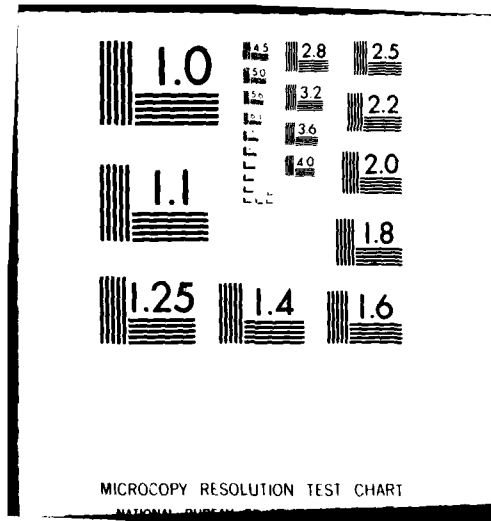
UNCLASSIFIED

NL

1 of 1  
AD  
AUG00 71



END  
DATE  
FILMED  
11-80  
DTIC



CADWALLENDER, KRAMER, JANKOWSKI and  
KISATSKY

AD A090371

FULL FIELD INTERFEROMETRY APPLICATIONS  
TO ARMY PROBLEMS

WILLIAM K. CADWALLENDER  
KIMBALL KRAMER  
PAUL Z. JANKOWSKI  
PAUL J. KISATSKY

US ARMY, ARADCOM, APPLIED SCIENCES DIVISION  
DOVER, NJ 07801

**INTRODUCTION:** A problem of considerable interest to the Army is the integrity of artillery projectile bodies. The Production Base Modernization Program for ammunition production calls for 100% testing of projectile bodies at high speeds. Traditional methods such as dye penetrant and magnetic particle inspection, and newer techniques such as ultrasonics and flux leakage methods are used to inspect items for cracks and flaws. All these methods have limitations and disadvantages such as long scan times, liquid immersion, and identification of non-structural surface defects.

Optical holography and the various forms of speckle interferometry, being sensitive to surface displacement or strain, tend to show only defects that adversely affect the strength of the shell wall, while not showing "cosmetic" defects. With appropriate configuration, the entire surface of a shell (360°) can be viewed and an easily interpretable "picture" readout of the defects can be provided.

We have, in the past, used standard double exposure holographic interferometry to inspect M393 projectiles and M483 projectiles (1). There are several alternative methods to conventional holography based on the phenomenon of laser speckle. Each offers advantages such as reduced vibration sensitivity and simplified fringe patterns, but have the disadvantage of reduced sensitivity (2,3). Among the most promising of these methods for implementation as a means of inspecting projectile metal parts is the speckle shearing method of Hung and Hovanesian (4,5). This method reveals fringes which are proportional to surface strains, not whole body motion. The method has seen limited employment in the testing of tires. We report here on its application to the testing of M483A1 projectile bodies.

This document is prepared  
for publication  
distribution

80 10 15 052

411842

DDC FILE COPY

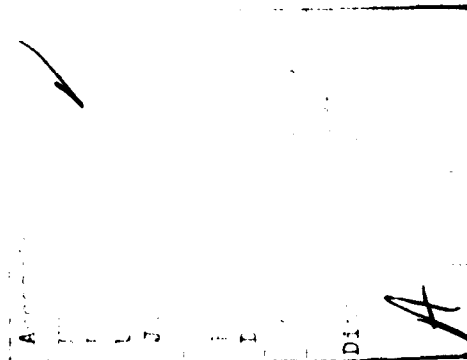
CADWALLENDER, KRAMER, JANKOWSKI and  
KISATSKY

**SPECKLE:** When an object is illuminated by a beam of coherent light such as a laser beam, the surface of the illuminated object takes on a grainy appearance which is termed speckle. This is true whether the illuminated beam is collimated or divergent and whether it originates directly from the laser or has been reflected from a specular surface or scattered from a diffusing surface. The grainy appearance is due to the fact that most surfaces are very rough when considered on the scale of optical wavelengths. When an area of the surface is viewed by the eye or any other optical system (camera, vidicon, etc.) the amplitude (and its square, the intensity) at a given point is a combination of the light coming from different elementary areas of the viewing surface. Because of the roughness of the viewing surface the light waves coming from different areas will have traveled slightly different distances, i.e., their optical paths will differ by a small number of wavelengths. If the light is coherent, there will be both constructive and destructive interference at the image plane (i.e., in the eye or camera) and a collection of random lighter and darker areas will manifest itself. This is speckle.

When an object being viewed is displaced laterally (in its own plane), the speckle pattern on the image plane is also displaced laterally. When the object is displaced axially (i.e., moved closer to or further from the imaging device), the speckles are shifted radially and magnified, and also gradually suffer a decorrelation. These movements of speckle patterns may be utilized to determine small displacements, deformations and strains in an object being viewed (6).

Speckle was first used to measure strain by Leendertz (2). The speckle strain techniques have several advantages over conventional double exposure holography: (a) Coherence demands are less stringent and thus the illuminating laser can often be run with multi-mode output, facilitating an increase in illumination levels and a decrease in necessary exposure time. (b) A modified conventional camera is used with its rather small lens aperture in contrast to conventional holography where an aperture at least the size of the plate to be exposed is needed. This makes it easier to use a narrow band transmission filter to block wavelengths other than that of the laser and thereby operate in ambient light rather than darkroom conditions. (c) By varying the camera aperture the speckle size can be varied as a function of the required resolution, and this can lead to the adoption of vidicon viewing and real-time applications.

The specific technique used in the studies discussed below uses a speckle interferometric camera developed by Hung & Liang (7). It has additional advantages: (d) The reference beam is split off at the recording device (camera) -- a so-called local reference beam -- and this reduces the vibration isolation demands of the system to the point where some work can be done on a standard laboratory table as opposed



to the vibration isolation tables necessary for conventional holography. (e) The technique gives derivatives of surface displacements directly, rather than displacements themselves, and these derivatives, being closely related to strain, reduce computation time and errors if strain is the parameter of interest. In this technique a local reference beam is created by using a wedge, i.e. a small angle prism, in front of half of the camera aperture. This results in a sheared image. Two sheared exposures are made, one before and one after the test object is stressed.

DESCRIPTION OF THE EXPERIMENTAL APPARATUS: The apparatus consists of a laser-illuminated object of interest, and a camera modified to have a thin glass wedge (i.e., a small angle prism) covering one-half of the lens aperture. The wedge angle is a parameter in the sensitivity of the technique and normally is in the 1 to 3 degree range.

We will define the z-axis to be the optical axis and choose the x-axis such that the laser lies in the x-z plane. We may visualize this as the camera, object and laser all lying in a horizontal plane with the object and camera defining the z-axis and the x-axis perpendicular to this. The y axis is thus vertical. The wedge is placed so that the wedge angle is in the x-z plane. Figure 1 is a schematic showing the arrangement looking down from above (along the y-axis).

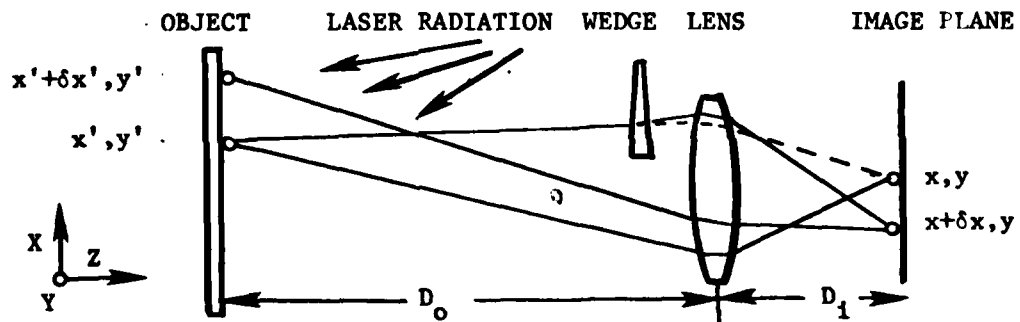


FIGURE 1

Those rays passing from the object to the image plane of the camera which do not pass thru the wedge will, of course, produce an image of the object. Those rays passing thru the wedge will produce an identical image of the object but displaced slightly ("sheared") in the x-direction. A developed image (single exposure) would look like a double exposure with the object moved slightly in the x direction between exposures. However in reality, the doubled image is made at one time by the shearing action of the wedge, and thus there is optical interference between the two parts of the sheared image. Note that this effect does not depend on collimation of the beam.

CADWALLENDER, KRAMER, JANKOWSKI and  
KISATSKY

**FRINGE FORMATION:** We have assumed that the wedge angle is in the  $x$ - $z$  plane and thus the two laterally sheared coherent images in the film plane correspond to an apparent shift of the object by  $\delta x$ . (The following analysis would hold, however, if the wedge were rotated by  $90^\circ$  and  $\delta y$  were substituted for  $\delta x$ .)

Let us consider two points on the object at  $x', y'$  and at  $x' + \delta x', y'$ . These are separated by the amount  $\delta x'$  on the object and are therefore imaged, in the absence of a wedge, on the film at  $x, y$  and  $x + \delta x, y$ , with the relationship between  $\delta x$  and  $\delta x'$  determined by the magnification factor  $M$ :

$$M = \delta x' / \delta x = D_1 / D_0$$

where  $D_1$  is the image-lens distance and  $D_0$  is the object-lens distance.

Let the wavefront of the unsheared image on the film plane corresponding to the object point  $x', y'$ , be:

$$U_{1A}(x, y) = A_{x, y} \exp(i \theta_{x, y})$$

and that corresponding to the object point  $x' + \delta x', y'$ , be:

$$U_{1B}(x + \delta x, y) = A_{x + \delta x, y} \exp(i \theta_{x + \delta x, y})$$

Here  $A$  is the amplitude and  $\theta$  is the phase of the wave.

We insert a small angle wedge or prism close to the lens with wedge angle  $\alpha$  and index of refraction  $\mu$  such that the image of the point  $x' + \delta x', y'$  is also imaged at  $x, y$  on the image (film) plane. Since the two waves are coherent and will interfere, the wavefront at the point  $x, y$  on the image plane is now the sum of  $U_{1A}(x, y)$ , above, and:

$$U_{1B}(x, y) = A_{x + \delta x, y} \exp[i(\theta_{x + \delta x, y} + 2\pi\gamma x / \lambda)]$$

where  $\gamma = \alpha(\mu - 1)$  is the angle of light deviation due to the prism (for small prism angles) (8). The factor  $2\pi\gamma x / \lambda$  enters because the wave  $U_{1B}$  is refracted by the prism thru the angle  $\gamma$  and is thus inclined with respect to  $U_{1A}$ .

We will assume that the amplitude  $A$  is independent of  $x$  and  $y$  for simplicity and to make clear the phase relationships. We then have the total wavefront (1st exposure only):

$$\begin{aligned} U_1(x, y) &= U_{1A}(x, y) + U_{1B}(x, y) \\ &= A \{ \exp[i \theta_{x, y}] + \exp[i(\theta_{x + \delta x, y} + 2\pi\gamma x / \lambda)] \} \end{aligned}$$

CADWALLENDER, KRAMER, JANKOWSKI and  
KISATSKY

Thus the intensity on the film due to the first exposure is:

$$I_1 = U_1 U_1^* = 2A^2 \{ 1 + \cos(\Delta\theta + 2\pi\gamma x/\lambda) \}$$

where  $\Delta\theta = \theta_{x+\delta x, y} - \theta_{x, y}$

Between the first and second exposures the object is deformed. We will again assume equal amplitudes at the second exposure. There is again interference, and we find almost the same intensity after deformation except for a small change due to the change of relative displacements between the points. This causes an additional small phase change  $\epsilon$ , and the intensity due to the second exposure is:

$$I_2 = 2A^2 \{ 1 + \cos(\Delta\theta + 2\pi\gamma x/\lambda + \epsilon) \}$$

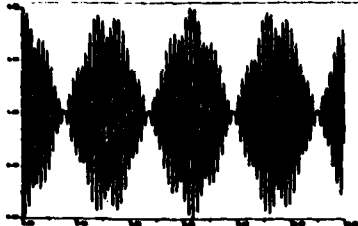
The two exposures are made at different times and there can be no interference between the wavefronts which produce  $I_1$  and  $I_2$ . Thus the total intensity at the point on the film (image plane) that we are considering is just the sum of the intensities due to the two exposures:

$$\begin{aligned} I &= I_1 + I_2 = 2A^2 \{ 2 + \cos(\Delta\theta + 2\pi\gamma x/\lambda) + \cos(\Delta\theta + 2\pi\gamma x/\lambda + \epsilon) \} \\ &= 4A^2 \{ 1 + \cos(\Delta\theta + 2\pi\gamma x/\lambda + \epsilon/2) \cdot \cos(\epsilon/2) \}. \end{aligned}$$

(This last equality is merely a trigonometric identity.) Note that if there is no deformation ( $\epsilon = 0$ ),  $I = 2I_1$ .

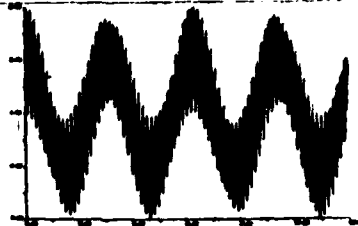
**FRINGE VISIBILITY:** The appearance of these intensity fringes depends on the relative magnitudes of the arguments of the cosine terms in the preceding equations. The factor describes a rapidly varying, randomly varying component which accounts for the observed speckle. This term will be neglected in the discussion which follows, which is designed to illustrate the types of fringes encountered and will not discuss the character of the superimposed speckle which is present in all cases. We will consider only the other two factors,  $2\pi\gamma x/\lambda$  and  $\epsilon$ . If the arguments in the upper equation are approximately the same, i.e.,  $2\pi\gamma x/\lambda \gg \epsilon$ , the fringe intensity varies as indicated in figure 2a. If the arguments in the upper equation are very different, i.e.,  $2\pi\gamma x/\lambda \ll \epsilon$ , the fringe intensity varies as indicated in figure 2b. In either case, if the eye can resolve the small fringes, we see rapid spatial variation of intensity with superimposed more slowly varying variations. However, if the resolution of the eye is not enough to resolve the small fringes, we see only a local average of the intensity, as plotted for the two cases in figures 2c and 2d.

$$4(1 + \{\cos(41x)\cos(1x)\})$$



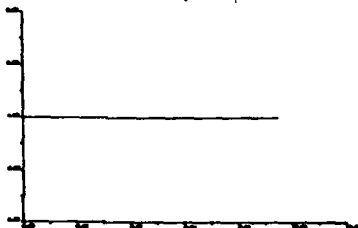
a

$$4(1 + \{\cos(21x)\cos(19x)\})$$



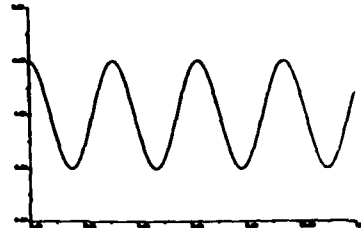
b

$$4$$



c

$$4 + 2\cos(2x)$$



d

e: Transform of 2a



Figure 2

CADWALLENDER, KRAMER, JANKOWSKI and  
KISATSKY

Unfortunately, it is the representation in figure 2a which corresponds to the results obtained with the speckle shearing technique. These fringes may be thought of as a high frequency carrier term modulated by a low frequency amplitude modulation. Alternatively we may think of the slowly varying envelope as moiré fringes resulting from superposition of two finer sets of fringes, one created by each exposure. By referring to the second equation describing the intensity variation, we can see that the slowly varying amplitude modulation is due to the cosine ( $\epsilon/2$ ) term and this must be made accessible to analyze the deformation which leads to the phase change  $\epsilon$ .

The necessary demodulation to render the low frequency spatial variation of intensity visible to the eye (or vidicon) may be accomplished by an optical Fourier transform and filtering technique.

The apparatus consists of: (a) a lens to perform the Fourier transform from the spatial domain to the frequency domain; (b) an opaque stencil for filtering; and (c) a second lens to re-transform the image back from the frequency domain to the spatial domain. To make the process clear, we will consider the demodulation of the light intensity distribution of figure 2a.

Figure 2e is the sum of the transforms of two cosine terms and a constant term. It shows the Fourier transform of the spatial light intensity distribution of figure and is thus the light intensity distribution at the focal plane. If we put an opaque stencil at this plane which (1) blocks out the center peak (this corresponds to a low frequency filter), and which (2) blocks out the two left side peaks, we are left with only the two right side peaks. When we retransform with the second lens, we operate only on the intensity distribution consisting of these two peaks and we have effectively shifted the origin to the point midway between them. The second lens thus performs the transform of the intensity distribution:  $1/2 \{ \delta(f - 1/2\pi) + \delta(f + 1/2\pi) \}$  which is  $\cos x$ . This is the modulation function separated from the term representing the carrier frequency in the original intensity distribution:

$$I = 4 \{ 1 + \cos(41x) \cdot (\cos x) \}.$$

When this retransformed image is viewed by the eye or a vidicon, the fringes due to the phase changes caused by the relative displacements between points,  $\epsilon$ , are visible. It remains to relate these to the strain.

RELATION OF FRINGES TO STRAIN: Following the analysis given in Ref. 7, we consider two points on an object to be investigated:  $P(x, y, z)$  which is displaced under strain to  $P'(x+u, y+v, z+w)$ , and  $P(x+\delta x, y, z)$  which is displaced under strain to  $P'(x+\delta x+u+\delta u, y+v+\delta v, z+w+\delta w)$ . We assume a laser source located at  $S(x_s, y_s, z_s)$  and an image point in the camera located at  $O(x_o, y_o, z_o)$  (figure 3):

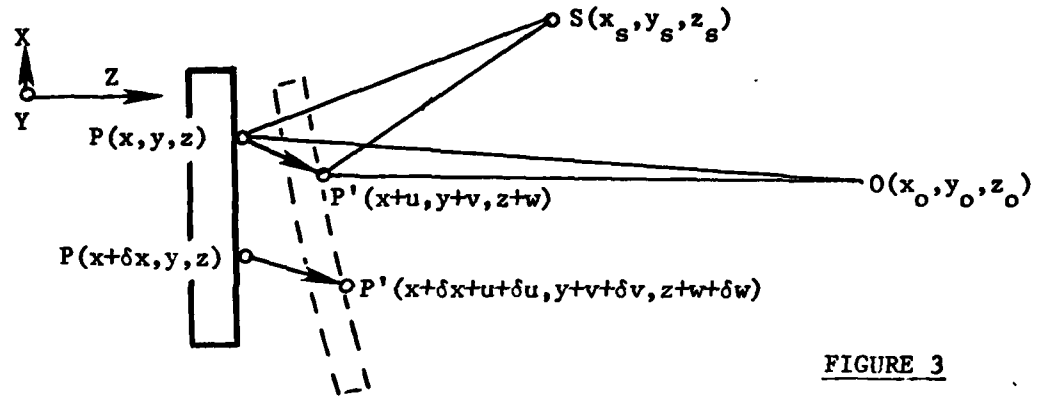


FIGURE 3

Let us consider the first of the two adjacent points. A light ray travels from S to P to O before deformation and from S to P' to O after deformation. The change in path length:

$$\delta l = (SP' + P'O) - (SP + PO)$$

can be shown to be (to first order):

$$\delta l = Au + Bv + Cw$$

$$\text{where } A = \frac{x - x_o}{R_o} + \frac{x - x_s}{R_s}$$

$$B = \frac{y - y_o}{R_o} + \frac{y - y_s}{R_s}$$

$$C = \frac{z - z_o}{R_o} + \frac{z - z_s}{R_s}$$

$$R_o^2 = x_o^2 + y_o^2 + z_o^2$$

$$R_s^2 = x_s^2 + y_s^2 + z_s^2$$

CADWALLENDER, KRAMER, JANKOWSKI and  
KISATSKY

Similarly the change in path length for a light ray which travels from the laser to the neighboring point to the camera is:

$$\delta l' = A(u + \delta u) + B(v + \delta v) + C(w + \delta w)$$

and the relative path change between the two points is:

$$r = A \delta u + B \delta v + C \delta w = (A \frac{\delta u}{\delta x} + B \frac{\delta v}{\delta x} + C \frac{\delta w}{\delta x}) \delta x.$$

The relative phase change is then:  $\epsilon = 2 \pi r / \lambda$

If  $\delta x$ , the amount of shearing, is small, we may approximately treat these small shifts as partial derivatives and rewrite the equation for the relative phase change:

$$\epsilon = \frac{2\pi}{\lambda} (A \frac{\partial u}{\partial x} + B \frac{\partial v}{\partial x} + C \frac{\partial w}{\partial x}) \delta x$$

The modulated intensity variations seen on the reconstructed image are due to variations of  $\epsilon$ . We see here that  $\epsilon$  is a function of the derivatives of the displacements in the shearing direction.

This expression for  $\epsilon$  is valid for the most general placement of the experimental apparatus. In practice, simplifying assumptions can be made. If the laser source and the camera lie in the x-z plane and the camera is on the z-axis, we have  $x_0 = y_0 = y_s = 0$ . If, in addition, the assumption that the object size is small compared with  $z_0$  and  $R_s$  is made, we have:

$$A \approx - \frac{x_s}{R_s} = - \sin \phi$$

$$B \approx 0$$

$$C \approx - (1 + \frac{z_s}{R_s}) = -(1 + \cos \phi)$$

Here the angle  $\phi$  is the angle between the incident and scattered laser beam, angle SPO.

With suitable reconstruction then, we see fringes due to the strain deformation of the form:

$$\epsilon = - \frac{2\pi}{\lambda} \{ (1 + \cos \phi) \frac{\partial w}{\partial x} + (\sin \phi) \frac{\partial u}{\partial x} \} \delta x$$

Similarly, if the incident laser beam is in the y-z plane with the shear remaining in the x direction, we see fringes:

$$\epsilon = - \frac{2\pi}{\lambda} \{ (1 + \cos \phi) \frac{\partial w}{\partial x} + (\sin \phi) \frac{\partial v}{\partial x} \} \delta x$$

CADWALLENDER, KRAMER, JANKOWSKI and  
KISATSKY

Finally, by analogy, the reconstructed fringes with the wedge rotated  $90^\circ$  to show displacement derivatives in the y direction are of the forms:

$$\epsilon = -\frac{2\pi}{\lambda} \left\{ (1 + \cos\phi) \frac{\partial w}{\partial y} + (\sin\phi) \frac{\partial u}{\partial y} \right\} \delta y \quad \text{and}$$

$$\epsilon = -\frac{2\pi}{\lambda} \left\{ (1 + \cos\phi) \frac{\partial w}{\partial y} + (\sin\phi) \frac{\partial v}{\partial y} \right\} \delta y$$

The strains of interest are conventionally:

$$\epsilon_x = \frac{\partial u}{\partial x}$$

$$\epsilon_y = \frac{\partial v}{\partial y}$$

$$\gamma = \frac{\partial u}{\partial y} + \frac{\partial v}{\partial x}$$

The relations between these and the displacement derivatives measured by the speckle shearing technique are readily apparent. If the in-plane strains themselves are needed, they may be deduced by using two different angles of laser illumination,  $\phi_1$ , and  $\phi_2$ , and solving the linear equation for the strain component needed. Out-of-plane strains may be easily obtained by using normal illumination ( $\phi = 0$ ), which gives  $\partial w / \partial x$  and  $\partial w / \partial y$  directly depending on the orientation of the shearing wedge.

**EXPERIMENTAL:** The shell body is placed in a fixture (figure 4) which seals the open ends of the body to permit stressing by pressure and also provides an axial load by means of a nut on the central post. An exposure is then made by the method outlined in the theory section, with the shell at atmospheric pressure. The shell is then stressed by pressurization with nitrogen (50-300 psi), and a second exposure made on the same plate. The plate is then developed and fixed in the normal manner and viewed in the image processor described above.

The direction of image shear can be at any angle to the axis of the shell, giving a set of fringes which are a map of strains in the direction of shear. We produced interferograms of all shells both with the shear along the axis of the shell (axial shear), and at right angles



CADWALLENDER, KRAMER, JANKOWSKI and  
KISATSKY

to the axis (transverse shear). We show here only the axially sheared interferograms as these show the defects most clearly. Interferograms of both directions of shear were made for three views of each shell ( $120^\circ$  apart) and at both 200 and 300 psi.

Severe problems can arise due to specular reflection. In particular exposure times are increased since most of the illumination is reflected specularly rather than scattered. Most of the shell bodies shown here were painted white to decrease exposure times but this is not necessary if care is taken with the experimental set-up.

We studied sixteen M483 projectile bodies. Four of these have artificial defects induced by electrical discharge machining. The remainder of the shells have apparent natural defects as determined by Magnaflux texting.

Figure 5a shows an interferogram of a good shell body at 300 psi. This is for reference and it can be seen that the fringes are relatively few and smooth. Figure 5b is an interferogram of an M483 with the keyway machined in. The interferogram shows that the keyway weakens the wall considerably, and a prominent and very confusing signature is generated. Finding defects in this area has proven virtually impossible.

The speckle shearing interferograms of four of the test shells with artificially machined defects of known depth are shown in Figures 6a to 6d. The locations are pointed out. For the most part the defect signatures were quite dramatic with the exception of the .080" internal defect in the nose of one test shell (figure 6d) which could not be seen at all, even at 300 psi.

Figures 7a to 7c show results from a selection of the shells with apparent natural defects. Figure 7a shows a shell with a split. Although the split is barely visible to the eye, it shows as a definite series of discontinuities in the fringe patterns. A continuation of this split appears in the base. Figure 7b shows a shell with a crack in the nose and Figure 7c a shell with a crack in the base. The "V's" in these signatures clearly point to the cracks.

SUMMARY AND CONCLUSIONS: A total of sixteen M483A1 projectile bodies were inspected using speckle shearing interferometry. Four had machined defects of known dimensions and the balance were Magnaflux rejects. Six shells were determined to have defects detectable by speckle shearing interferometry, and the remaining six had keyway defects. All machined defects were located, with the sole exception of the .080" internal defects in the nose of one test shell which could not be seen even at 300 psi.

All other defects in the sample could be seen with pressures of no more than 200 psi. Problems encountered included specular reflections which could be minimized by careful arrangement, and the problem

CADWALLENDER, KRAMER, JANKOWSKI and  
KISATSKY

of the keyway signature, which could be avoided by inspecting before  
the keyway was cut.

BIBLIOGRAPHY:

1. Barbarisi, Modesto J., and Robert A. Barusefski, Double Exposure Holographic Examination of Projectile 105mm HEP-T-M393A2 For Flaws and Cracks, Feltman Research Laboratories, 1976.
2. Leendertz, J. A., J. Phys. E 3, 214-18 (1970).
3. Archbold, E., J. M. Burch, and A. E. Ennos, Optica Acta 17 (12), 883-898 (1970).
4. Hung, Y. Y., and J. O. Hovanesian, Exper. Mech. 12 (10), 454-460 (1972).
5. Hung, Y. Y., and A. J. Durelli, Simultaneous Determination of Three Strain Components in Speckle Interferometry Using a Multiple Image Shearing Camera, Final report on O. U. Project 32110-18, Grant # EN677-07974, Oakland University, 1978.
6. Erf, R. K., ed., Speckle Metrology, Academic Press, New York 1978.
7. Hung, Y. Y., and C. Y. Liang, Appl. Optics 18, 1046-1051 (1979).
8. Ditchburn, R. W., Light, 3rd ed., Academic Press, New York, 1976, pp. 55-57.



a- no defects



b- keyway

Figure 5

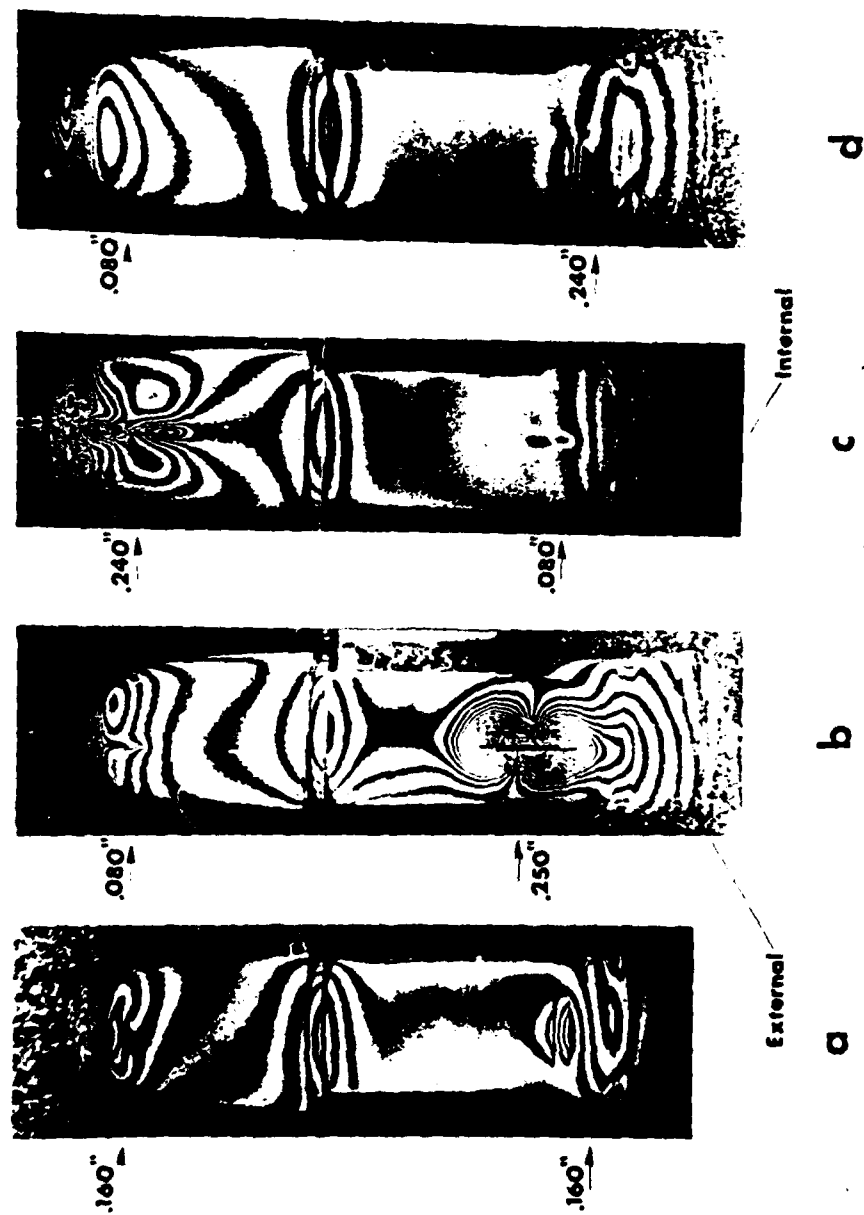


Figure 6 Artificial Defects

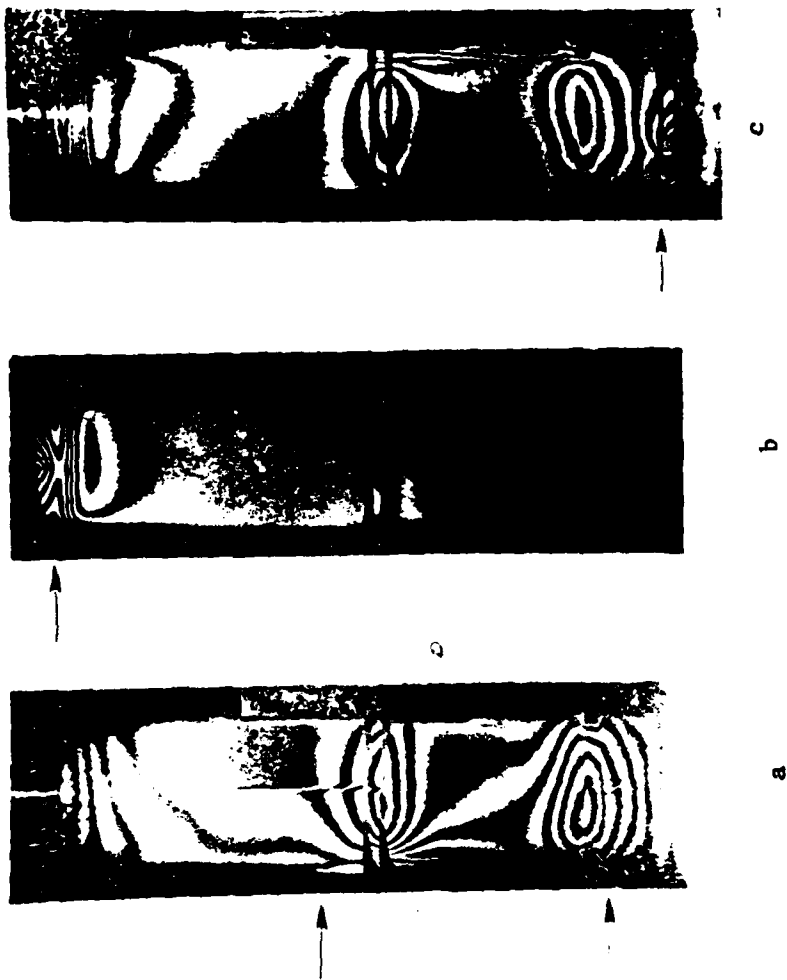


Figure 7 Natural Defects